

See discussions, stats, and author profiles for this publication at: <https://www.researchgate.net/publication/267342087>

# Extraordinary role of Hg in enhancing the thermoelectric performance of p-type SnTe

ARTICLE *in* ENERGY & ENVIRONMENTAL SCIENCE · OCTOBER 2015

Impact Factor: 20.52 · DOI: 10.1039/C4EE01463D

CITATIONS

16

READS

226

10 AUTHORS, INCLUDING:



**Tan Gangjian**

Northwestern University

32 PUBLICATIONS 427 CITATIONS

SEE PROFILE



**Jeff W Doak**

Northwestern University

14 PUBLICATIONS 163 CITATIONS

SEE PROFILE



**Hui Sun**

Michigan State University

7 PUBLICATIONS 34 CITATIONS

SEE PROFILE



**Lidong Zhao**

Université Paris-Sud 11

94 PUBLICATIONS 2,157 CITATIONS

SEE PROFILE



Cite this: *Energy Environ. Sci.*, 2015, 8, 267

## Extraordinary role of Hg in enhancing the thermoelectric performance of p-type SnTe†

Gangjian Tan,<sup>‡a</sup> Fengyuan Shi,<sup>‡b</sup> Jeff W. Doak,<sup>‡b</sup> Hui Sun,<sup>‡c</sup> Li-Dong Zhao,<sup>‡a</sup> Pengli Wang,<sup>‡a</sup> Ctirad Uher,<sup>‡c</sup> Chris Wolverton,<sup>‡b</sup> Vinayak P. Dravid<sup>‡b</sup> and Mercouri G. Kanatzidis<sup>‡\*ad</sup>

We report several synergistic effects in Hg alloying of SnTe to enhance the power factor and overall figure of merit  $ZT$ . Hg alloying decreases the energy separation between the two valence bands, leading to pronounced band convergence that improves the Seebeck coefficient. Hg alloying of SnTe also significantly enlarges the band gap thereby effectively suppressing the bipolar diffusion. Collectively, this results in high  $ZT$  of  $\sim 1.35$  at 910 K for 2% Bi-doped SnTe with 3%HgTe. The solubility limit of Hg in SnTe is less than 3 mol%, and above this level we observe HgTe precipitates in the SnTe matrix, typically trapped at grain boundary triple junctions. The strong point defect scattering of phonons caused by Hg alloying coupled with mesoscale scattering via grain boundaries contributes to a great reduction of lattice thermal conductivity. The multiple synergistic roles that Hg plays in regulating the electron and phonon transport in SnTe provide important new insights into continued optimization of SnTe-based and related materials.

Received 11th May 2014  
Accepted 25th September 2014

DOI: 10.1039/c4ee01463d

www.rsc.org/ees

### Broader context

Band engineering is an efficient way of enhancing the thermoelectric performance of typical semiconductors. It usually incorporates resonant levels, band degeneracy, and band gap tuning through chemical doping approaches. Herein we show that a tiny amount of HgTe alloying could not only significantly diminish the energy separation between the two valence bands in SnTe, leading to enhanced Seebeck coefficient, but notably enlarge the band gap of SnTe, giving rise to suppressed bipolar diffusion. The considerable point defect scattering by Hg alloying in combination with excess HgTe forming mesoscale structures results in great reduction in the lattice thermal conductivity. The synergistic role that Hg plays in SnTe leads to a record high  $ZT$  of 1.35 at 910 K.

<sup>a</sup>Department of Chemistry, Northwestern University, Evanston, Illinois 60208, USA.  
E-mail: m-kanatzidis@northwestern.edu

<sup>b</sup>Department of Materials Science and Engineering, Northwestern University, Evanston, Illinois 60208, USA

<sup>c</sup>Department of Physics, University of Michigan, Ann Arbor, Michigan 48109, USA

<sup>d</sup>Materials Science Division, Argonne National Laboratory, Argonne, Illinois 60439, USA

† Electronic supplementary information (ESI) available: Room temperature densities for all the samples investigated in this study (Table S1); powder XRD pattern of as-synthesized HgTe (Fig. S1); thermal diffusivity, heat capacity, and Lorenz number for  $\text{Sn}_{0.98}\text{Bi}_{0.02}\text{Te}-x\%\text{HgTe}/\text{CdTe}$  samples (Fig. S2); powder XRD pattern of  $\text{Sn}_{0.98}\text{Bi}_{0.02}\text{Te}-x\%\text{CdTe}$  (Fig. S3); temperature dependent thermoelectric transport properties for  $\text{Sn}_{0.98}\text{Bi}_{0.02}\text{Te}-x\%\text{CdTe}$  (Fig. S4); Electronic absorption spectra for  $\text{Sn}_{0.98}\text{Bi}_{0.02}\text{Te}-x\%(\text{Hg},\text{Cd})\text{Te}$  (Fig. S5); STEM EDS spectrum image of  $\text{Sn}_{0.98}\text{Bi}_{0.02}\text{Te}-3\%\text{HgTe}$  (Fig. S6); temperature dependent thermoelectric transport properties for  $\text{Sn}_{0.98}\text{Bi}_{0.02}\text{Te}-3\%\text{HgTe}$  before and after a 723 K–7 d vacuum annealing treatment (Fig. S7). See DOI: 10.1039/c4ee01463d

‡ G.J.T. and M.G.K. conceived of and planned the experiments. G.J.T. synthesized the samples, carried out and analyzed thermoelectric experiments. F.Y.S. and V.P.D. performed the TEM characterizations J.W.D. and C.W. carried out the band structure calculations. H.S. and C.U. carried out the Hall measurements. L.D.Z. and P.L.W. helped with sample synthesis. G.J.T., F.Y.S., J.W.D., H.S., L.D.Z., P.L.W., C.U., C.W., V.P.D. and M.G.K. conceived the experiments, analyzed the results and co-edited the manuscript.

## 1. Introduction

Thermoelectric materials, capable of realizing the direct conversion between heat and electricity, have received worldwide attention due to their potential in playing a role in energy efficiency.<sup>1–6</sup> Materials systems that can operate around 500–900 K are particularly attractive because most of the waste heat in industry and automobile exhaust is within this range.<sup>7–9</sup> To date, the leading materials are lead chalcogenides,<sup>10–17</sup> filled skutterudites,<sup>18–22</sup> and some diamond-like compounds.<sup>23–25</sup> Several advances in this field have been achieved in PbTe-based materials with the highest figure of merit  $ZT$  exceeding 2 at 915 K. This was accomplished by synergistically applying the concepts of band structure engineering and microstructure modification (panoscopic approach).<sup>12,26</sup> Although lead chalcogenides have been extensively studied, their Sn-based analogues especially SnTe which is similar to PbTe in regards to crystal structure, crystal chemistry and general doping principles did not receive significant attention.<sup>27–30</sup>

The main drawbacks of SnTe are the smaller band gap (0.18 eV at 300 K) and much larger energy separation (0.35 eV at 300

K) between the light-hole band at  $L$  point and heavy-hole band at  $\Sigma$  point with respect to PbTe (0.30 eV and 0.17 eV at 300 K, respectively).<sup>26,27,31,32</sup> These result in significant bipolar conduction and lower Seebeck coefficient for SnTe when compared to PbTe at a similar carrier density level, and consequently SnTe exhibits considerably inferior thermoelectric performance. Attempts at modifying the valence band structure of SnTe have been made to improve its  $ZT$  value. Zhang *et al.*<sup>27</sup> reported a resonant level near the Fermi level of SnTe introduced by indium doping and found a prominent enhancement of the Seebeck coefficient. In conjunction with a successful reduction of thermal conductivity through refined microstructure by ball milling, they reported a  $ZT$  of  $\sim 1.1$  around 873 K. Recently, we reported that Cd as an alloying element favorably impacts the band structure of SnTe in two aspects: (a) band gap enlargement and (b) valence band convergence, leading to suppressed bipolar diffusion and increased Seebeck coefficient. Concurrently, utilizing CdS/ZnS nanoscale precipitates as strong phonon scattering features, the lattice thermal conductivity of SnTe is considerably decreased. As a consequence, a maximum  $ZT$  of  $\sim 1.3$  at  $\sim 873$  K was achieved.<sup>33</sup> These findings make SnTe-based materials a robust candidate for thermoelectric power generation application and warrant further investigation and optimization.

In this study, we explored another group 14 element, Hg, as a possible alloying addition for SnTe, with Bi as the electron donor dopant. Compared to Cd, Hg has additional advantages. Our experimental results and theoretical calculations unambiguously reveal that Hg is more efficient in producing valence band degeneracy than Cd. Moreover, the  $\text{Sn}_{1-x}\text{Hg}_x\text{Te}$  samples exhibit lower lattice thermal conductivities than Cd-containing samples with comparable Hg and Cd concentration levels. When the Hg content exceeds its solubility of  $\sim 2\text{--}3$  mol%, large and isolated HgTe particles were found preferentially at grain boundaries and triple junctions, which are unlikely to contribute to any notable or effective phonon scattering. Therefore, we suggest that the point defects in the matrix created by Hg alloying are the primary reason for the lower lattice thermal conductivity in the HgTe containing samples, with expected smaller contribution from mesoscale grain boundaries. As a result, a high  $ZT$  of  $\sim 1.35$  at  $\sim 910$  K was obtained for the sample with nominal composition  $\text{Sn}_{0.98}\text{Bi}_{0.02}\text{Te}\text{--}3\%\text{HgTe}$ , which is comparable to that of Cd-alloyed SnTe nanostructured with CdS. However, a much higher average  $ZT$  ( $ZT_{\text{ave}}$ ) exceeding unity between 500 and 900 K is found in the Hg-alloyed samples, making them superior to the Cd-containing system.

## 2. Experimental procedures

### Synthesis

Reagent chemicals were used as obtained: Sn chunk (99.9999%, American Elements, US), Bi shot (99.999%, American Elements, US), Cd shot (99.99%, Alfa, US), Hg liquid (99.99%, Baker, US), and Te shot (99.999%, 5 N Plus, Canada).

**Synthesis of starting materials.** HgTe was synthesized by direct reaction between Hg and Te. About 2 g of Hg liquid was

carefully weighed using a pipette and transferred into a 10 mm diameter silica tube by the use of weighing paper. The desired amount of Te was then weighed and mixed with Hg. The tube was evacuated to a pressure of  $\sim 10^{-4}$  Torr and flame-sealed. During the evacuation process, make sure the bottom of the tube was totally immersed in the liquid nitrogen so that the Hg was concretionary in case that it got vaporized. The sealed tube was then vertically placed into a computer controlled furnace and heated up to 773 K, dwelled at this temperature for 10 h, and then cooled down to room temperature by turning off the furnace power. Such a heating-cooling process was repeated several times to ensure the complete reaction and good homogeneity of the product. The phase composition of the resultant product was checked by powder XRD, which showed that pure phase HgTe could be successfully synthesized by this method, see ESI (Fig. S1†).

Samples with nominal compositions  $\text{Sn}_{0.98}\text{Bi}_{0.02}\text{Te}\text{--}x\%\text{HgTe}$  ( $x = 0, 0.5, 1, 2, 3$ , and 4, in mole fraction) and two control samples  $\text{Sn}_{0.98}\text{Bi}_{0.02}\text{Te}\text{--}x\%\text{CdTe}$  ( $x = 2$  and 3, in mole fraction) were prepared as follows. Appropriate amounts of Sn, Bi, HgTe, Cd, and Te were weighed and mixed in 10 mm diameter silica tubes. The tubes were then evacuated to a residual pressure of  $\sim 10^{-4}$  Torr, flame-sealed, slowly heated to 1273 K, soaked at this temperature for 8 h, and quickly cooled to room temperature by water quenching. The resultant ingots were resealed in 13 mm diameter silica tubes and vacuum annealed at 673 K for 12 h, and then slowly cooled to room temperature by switching off the furnace power. For a typical experiment: Sn (3.6540 g, 30.7862 mmol), Bi (0.1313 g, 0.6283 mmol), HgTe (0.2062 g, 0.6283 mmol), and Te (4.0085 g, 31.4145 mmol) were used to prepare 8 g of  $\text{Sn}_{0.98}\text{Bi}_{0.02}\text{Te}\text{--}2\%\text{HgTe}$ .

The melt grown ingots were ground into fine powders using a mechanical mortar and pestle to reduce the grains to less than 4  $\mu\text{m}$  in diameter. These powders were then densified by spark plasma sintering (SPS) method (SPS-211LX, Fuji Electronic Industrial Co., Ltd.) at 773 K for 5 min in a 12.7 mm diameter graphite die under an axial pressure of 40 MPa in vacuum. Highly dense ( $>97\%$  of theoretical density, Table S1†) disk-shaped pellets with dimensions of 12.7 mm diameter and 8 mm thickness were obtained.

### Physical characterization

**Electrical properties.** The SPSed pellets were cut into 12 mm  $\times$  3 mm  $\times$  3 mm bars for simultaneous measurement of the Seebeck coefficient and the electrical conductivity using an Ulvac Riko ZEM-3 instrument under a low-pressure helium atmosphere from room temperature to 823 or 923 K. Samples were spray coated with boron nitride spray to minimize outgassing except where needed for electrical contact with the thermocouples, heater, and voltage probes. The uncertainty of the Seebeck coefficient and electrical conductivity measurements is 5%.

**Thermal conductivity.** The SPSed pellets were cut and polished into a squared shape of 6  $\times$  6  $\times$  2 mm<sup>3</sup> for thermal diffusivity measurements. The thermal diffusivity coefficient ( $D$ ) was measured using the laser flash diffusivity method in a

Netzsch LFA457, the specific heat capacity ( $C_p$ ) was indirectly derived using a representative sample (Pyroceram 9606) in the range 300–923 K, and the density ( $d$ ) was determined using the dimensions and mass of the sample. The thermal conductivity was calculated from  $\kappa = DC_p d$ . The uncertainty of the thermal conductivity is estimated to be within 8%, considering the uncertainties from  $D$ ,  $C_p$ , and  $d$ . The thermal diffusion and the heat capacity data for all samples can be found in the ESI (Fig. S2†). The combined uncertainty for all measurements involved in the calculation of  $ZT$  is less than 15%. No directional anisotropy effects were observed in the charge transport properties.

**Hall measurements.** The Hall measurement was performed on homemade apparatuses (University of Michigan). The low temperature portion between 5 and 300 K was carried out in a cryostat equipped with a radiation shield using a Linear Research ac bridge with 16 Hz excitation in a magnet cryostat capable of fields up to 5 T. For the high temperature portion (300 to  $\sim 873$  K), the samples were press mounted and protected with argon gas to avoid possible oxidization at high temperature. The Hall resistance was monitored with a Linear Research AC Resistance Bridge (LR-700), with constant magnetic fields of  $\pm 1$  T applied by using an Oxford Superconducting magnet.

**Band gap measurements.** Room temperature optical diffuse reflectance measurements were performed on finely ground powders to probe optical energy gap of the series. The spectra were collected in the mid-IR range (6000–400  $\text{cm}^{-1}$ ) using a Nicolet 6700 FT-IR spectrometer. The reflectance *versus* wavelength data generated, were used to estimate the band gap by converting reflectance to absorption data according to Kubelka–Munk equations:  $\alpha/S = (1 - R)^2/(2R)$ , where  $R$  is the reflectance,  $\alpha$  and  $S$  are the absorption and scattering coefficients, respectively. The results are shown in Fig. S5.†

### Electron microscopy and X-ray diffraction

Scanning and scanning transmission electron microscopy (STEM) investigations were carried out in a JEOL 2100F microscope operated at 200 kV. STEM energy dispersion spectroscopy (EDS) spectrum imaging (SI) was carried out with a Hitachi HD-2300 dedicated STEM equipped with high collection angle dual EDS detectors. Thin TEM specimens were prepared by conventional methods, including cutting, grinding, dimpling, tripod, with minimal duration of Ar-ion milling, and followed by liquid nitrogen cooled, low energy (900 eV) ion milling by Fischione Nanomill. Samples pulverized with an agate mortar were used for powder X-ray diffraction (XRD). The powder diffraction patterns were obtained with Cu  $K_\alpha$  ( $\lambda = 1.5418$  Å) radiation in a reflection geometry on an INEL diffractometer operating at 40 kV and 20 mA and equipped with a position-sensitive detector.

### Band structure calculations

Density functional theory (DFT)<sup>34,35</sup> calculations of the band structures of SnTe, Cd-doped SnTe, and Hg-doped SnTe were carried out using the Vienna *Ab initio* Simulation Package (VASP).<sup>36–39</sup> Calculations were performed with projector-augmented wave (PAW)<sup>40</sup> potentials and the exchange-

correlation functional of Perdew, Burke, and Erzenhoff (PBE)<sup>41</sup> using spin-orbit coupling (SOC). Potentials for Sn, Cd, Hg, and Te, contained the  $4d^{10}5s^25p^2$ ,  $4d^{10}5s^2$ ,  $5d^{10}6s^2$ , and  $5s^25p^4$  electrons as valence, respectively.<sup>42</sup> Cd- and Hg-doped SnTe calculations were performed on 54-atom supercells created by replacing 1 Sn atom with either Cd or Hg in a  $3 \times 3 \times 3$  supercell of the rocksalt primitive cell of SnTe. There is no ambiguity in the choice of the Sn site for Hg or Cd substitution because all 27 Sn atoms in the 54-atom supercell are symmetrically equivalent. The pure SnTe supercell and doped supercells were relaxed using the relaxation scheme of the Open Quantum Materials Database (OQMD),<sup>43</sup> with a subsequent relaxation with 520 eV plane-wave basis cutoff energies,  $5 \times 5 \times 5$   $\Gamma$ -centered  $k$ -point meshes, and tetrahedral  $k$ -point integration. Band structure calculations were performed for each of the supercells using 520 eV cutoff energies and 20  $k$ -points along each of the lines from  $L$  to  $\Gamma$  and from  $\Gamma$  to  $K$  in the 54-atom rocksalt supercell Brillouin Zone.

The electron eigenvalues of the Cd- and Hg-doped SnTe band structures were aligned to the electron eigenvalues of the pure SnTe band structure through an alignment procedure making use of the electrostatic potentials of the pure and doped supercells.<sup>44</sup> The electrostatic potential was averaged around each atom in the pure, Cd-, and Hg-doped supercells. The difference between these atom-averaged electrostatic potentials in the doped and pure supercells were taken and averaged over each atom lying outside a sphere with a radius of one half the defect (Cd or Hg) periodic image distance, centered at the defect. Subtracting this cell-averaged electrostatic potential difference from the electron eigenvalues of the defect supercells aligns the band structure of the defected supercells with the band structure of the pure SnTe supercell, placing the band structures on the same energy scale and allowing for accurate comparisons between the band structures of pure, Cd-, and Hg-doped SnTe.

## 3. Results and discussion

### Solubility limit of HgTe in 2 mol% Bi-doped SnTe

The PXRD patterns for samples of  $\text{Sn}_{0.98}\text{Bi}_{0.02}\text{Te}-x\%\text{HgTe}$  show NaCl-type structure as the main phase for all samples and for  $x \geq 3$  a trace amount of cubic HgTe as a second phase, Fig. 1(a). Similarly, we find that one of the control samples (alloying with Cd)  $\text{Sn}_{0.98}\text{Bi}_{0.02}\text{Te}-2\%\text{CdTe}$  shows single phase while at 3% CdTe we observe a trace of CdTe as a second phase, see ESI (Fig. S3†). As can be seen from Fig. 1(b), the lattice parameter increases with increasing  $x$  until  $x = 2$  and beyond that it saturates. The increase in SnTe lattice parameter upon HgTe alloying is consistent with the fact  $\text{Hg}^{2+}$  (ionic radius 0.110 nm) is larger than  $\text{Sn}^{2+}$  (0.093 nm). The measured room temperature hole density is plotted in Fig. 1(c), which shows an increasing trend with increasing  $x$ , although Hg is supposed to be isovalent with Sn. The hole mobility, however, decreases with increasing  $x$ , Fig. 1(d), probably due to alloy scattering, and higher effective mass of holes caused by band structure modification, which we will discuss later. Collectively, both the lattice parameter and hole density variations suggest that the solubility limit of HgTe

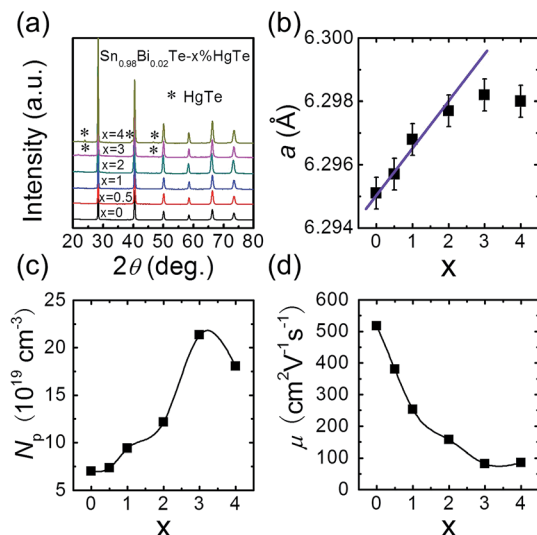


Fig. 1 Room temperature (a) powder XRD patterns, (b) lattice parameter  $a$ , (c) Hall carrier density  $N_p$ , and (d) carrier mobility  $\mu$  for  $\text{Sn}_{0.98}\text{Bi}_{0.02}\text{Te}-x\%\text{HgTe}$  samples. The solid line in (b) is a guide to eye.

in  $\text{Sn}_{0.98}\text{Bi}_{0.02}\text{Te}$  is between 2% and 3%, which is higher than the  $\sim 1.5$  mol% observed by Nasirov *et al.*<sup>45</sup>

### Electrical transport properties

Fig. 2(a) shows the electrical conductivity as a function of temperature for  $\text{Sn}_{0.98}\text{Bi}_{0.02}\text{Te}-x\%\text{HgTe}$ . Clearly, the room temperature electrical conductivity decreases significantly from  $\sim 5815 \text{ S cm}^{-1}$  in  $\text{Sn}_{0.98}\text{Bi}_{0.02}\text{Te}$  to  $\sim 2467 \text{ S cm}^{-1}$  for the sample with 4%HgTe. This reduction in electrical conductivity is mainly attributed to the decrease in carrier mobility, Fig. 1(d). Similar to the case of PbTe and PbSe,<sup>46,47</sup> modeling the electrical

conductivity of SnTe-based materials with a single power law dependence of the form  $\sigma \sim T^{-\delta}$  is inadequate. Instead, two distinct regions with two different  $\delta$  ( $\delta_1$  in the low temperature range and  $\delta_2$  in the high temperature range) values can be extracted from the  $\ln \sigma - \ln T$  plot, Fig. 2(b). The inset of Fig. 2(b) shows plots  $\delta_1$  and  $\delta_2$  as a function of  $x$ , both of which decrease evidently with increasing HgTe content. The much smaller  $\delta$  values in the HgTe-containing samples imply a much weaker temperature dependence of hole scattering at high temperature. Therefore, at high temperature, these samples have comparable or even higher electrical conductivities than the  $\text{Sn}_{0.98}\text{Bi}_{0.02}\text{Te}$  sample, even if their room temperature electrical conductivities are significantly lower, Fig. 2(a).

Contrary to the behavior of the electrical conductivity, the room temperature Seebeck coefficient increases prominently with increasing amounts of HgTe, from  $\sim 22.1 \mu\text{V K}^{-1}$  for  $\text{Sn}_{0.98}\text{Bi}_{0.02}\text{Te}$  to  $\sim 66.8 \mu\text{V K}^{-1}$  for the sample with 4%HgTe despite the gradually increased hole density, Fig. 2(c). It should be noted that although the Seebeck coefficients of the HgTe-containing samples are enhanced with respect to the pristine  $\text{Sn}_{0.98}\text{Bi}_{0.02}\text{Te}$  over the entire temperature range, the improvement becomes less dramatic at higher temperatures. Thus, benefiting from the simultaneous enhancement of electrical conductivity and Seebeck coefficient at high temperatures, the HgTe-containing samples have much higher power factors than the pristine  $\text{Sn}_{0.98}\text{Bi}_{0.02}\text{Te}$  samples, with maximum values exceeding  $\sim 27 \mu\text{W cm}^{-1} \text{ K}^{-2}$ , Fig. 2(d). This is the highest power factor value reported so far for SnTe-based materials.<sup>27,33</sup>

### Valence band convergence by HgTe alloying

To shed more light on the variation of the Seebeck coefficient, it is useful to compare the room temperature  $S$  vs.  $N_p$  plot for  $\text{Sn}_{0.98}\text{Bi}_{0.02}\text{Te}-x\%\text{HgTe}$  with the well-established Pisarenko plot obtained from a single valence band model (VBM),<sup>27</sup> Fig. 3. The data points for  $\text{Sn}_{0.98}\text{Bi}_{0.02}\text{Te}$  in this study, together with those of previously reported Bi-doped<sup>48,49</sup> and non-doped SnTe samples,<sup>31,50</sup> fall exactly on the Pisarenko plot, consistent with the previous report that Bi is a simple dopant in SnTe.<sup>27</sup>

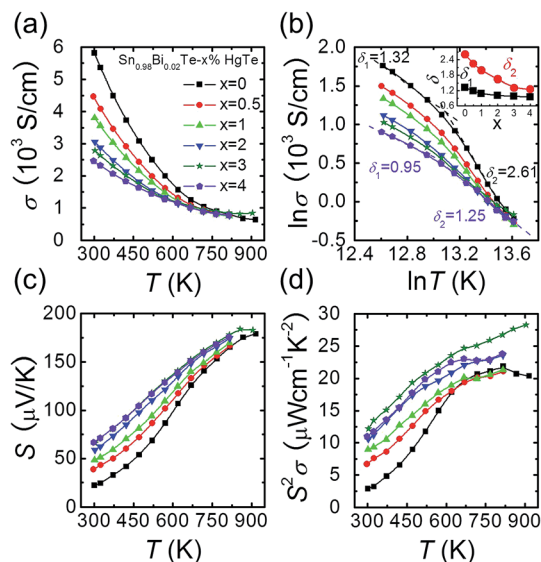


Fig. 2 Temperature dependent (a) electrical conductivity  $\sigma$ , (c) Seebeck coefficient  $S$ , and (d) power factors  $S^2\sigma$  for  $\text{Sn}_{0.98}\text{Bi}_{0.02}\text{Te}-x\%\text{HgTe}$  samples; (b):  $\ln \sigma$  as a function of  $\ln T$  to extract the exponential factor  $\delta$  in the form of  $\sigma \sim T^{-\delta}$ ; inset of (b):  $x$  dependent  $\delta$  values.

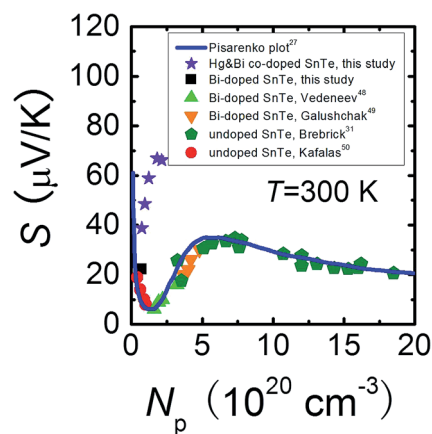


Fig. 3 Room temperature Pisarenko plot for  $\text{Sn}_{0.98}\text{Bi}_{0.02}\text{Te}-x\%\text{HgTe}$  samples in comparison with reported data on Bi-doped<sup>48,49</sup> and undoped SnTe.<sup>31,50</sup> The solid line is based on the VBM model.<sup>27</sup>



However, the Seebeck coefficients of the Hg-alloyed samples are far higher than the theoretical prediction, similar to the cases in Cd-doped<sup>33</sup> and In-doped<sup>27</sup> SnTe, which were reported to arise from the valence band convergence induced by Cd doping<sup>33</sup> and the resonant level introduced by In doping<sup>27</sup> respectively. Considering the analogous electronic properties of Cd and Hg, we deduce that a similar valence band convergence could happen in HgTe-alloyed SnTe. Indeed, with similar hole densities, the  $\text{Sn}_{0.98}\text{Bi}_{0.02}\text{Te}$  with 0.5% HgTe ( $7.34 \times 10^{19} \text{ cm}^{-3}$ ,  $\sim 38.7 \mu\text{V K}^{-1}$ ) has a comparable Seebeck coefficient with that of 2% Cd-doped SnTe ( $6.85 \times 10^{19} \text{ cm}^{-3}$ ,  $\sim 45.4 \mu\text{V K}^{-1}$ ) at room temperature,<sup>33</sup> suggesting their similarity in valence band structure. However, the same level of band convergence can be produced by an apparent lower doping amount of Hg, indicating that Hg is more efficient than Cd in minimizing the energy separation between the two valence bands which also can be demonstrated by the band structure calculations.

We examined this hypothesis of band convergence with DFT calculations. Fig. 4(a)–(c) show the DFT band structures of pristine SnTe, Cd-doped, and Hg-doped SnTe respectively along the lines  $L$  to  $\Gamma$  and  $\Gamma$  to  $K$  in the rocksalt BZ. It can be seen that the energy separation between the light-hole band and heavy-hole band extrema ( $\Delta\epsilon$ ) for the Cd-doped and Hg-doped SnTe is significantly reduced relative to the pristine SnTe. Furthermore, the decrease in  $\Delta\epsilon$  is more pronounced in Hg-doped SnTe than in Cd-doped SnTe, consistent with our experimental observations. Moreover, the band gap,  $E_g$ , of

SnTe is significantly enlarged upon Cd or Hg alloying. This band gap enlargement is beneficial to suppressing the bipolar diffusion which will be discussed later. Specifically,  $\Delta\epsilon$  are 0.24, 0.10, and 0.06 eV, while  $E_g$  are 0.12, 0.41, and 0.39 eV at 0 K for pure SnTe, Cd-doped, and Hg-doped SnTe respectively, as shown in Fig. 4(d). The calculated band gap of pure SnTe (0.12 eV) is in good agreement with previous calculated values (0.11 eV (ref. 51) and 0.212 eV (ref. 52)), and slightly smaller than the experimentally determined band gap (0.3 eV at 4 K (ref. 53), and 0.18 eV at 300 K (ref. 54)). Calculations of Cd-doped SnTe have been performed previously, and we find good agreement with their electronic structure.<sup>55</sup> We find the trends in DFT-calculated band gaps and light-hole–heavy-hole energy separations agree well with the experimental observations. Specifically, we have measured electronic absorption spectra for  $\text{Sn}_{0.98}\text{Bi}_{0.02}\text{Te}-x\%(\text{Hg},\text{Cd})\text{Te}$ , shown in Fig. S5.† Although specific band gaps cannot be derived from the spectra because of the strong interference from a large amount of free carriers,<sup>33</sup> the gradual shift of the absorption edges towards higher energy region upon Hg/Cd alloying indicates an increase of band gap upon alloying.

The temperature dependent Hall data analysis can further support the band convergence hypothesis. Fig. 5(a) shows the temperature dependent Hall coefficient  $R_H$  for three pure phase samples  $\text{Sn}_{0.98}\text{Bi}_{0.02}\text{Te}$ ,  $\text{Sn}_{0.98}\text{Bi}_{0.02}\text{Te}-2\%\text{HgTe}$ , and  $\text{Sn}_{0.98}\text{Bi}_{0.02}\text{Te}-2\%\text{CdTe}$ .  $R_H$  is almost constant (less than 10% variation) below 150 K because when the temperatures are

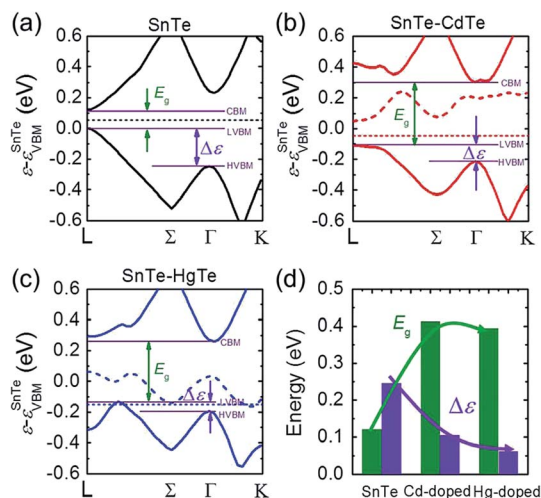


Fig. 4 DFT band structures for (a) pure SnTe, (b) Cd-doped SnTe, and (c) Hg-doped SnTe, all shown relative to the VBM of pure SnTe. The thickest solid lines show the valence and conduction bands of each system, dashed lines show the defect bands formed when Cd or Hg is substituted for Sn in SnTe, and the horizontal dotted lines show the 0 K Fermi level for each system. The horizontal purple solid lines from top to bottom correspond to the energies of conduction band minima (CBM), light valence band maxima (LVBM) and heavy valence band maxima (HVBM), respectively. The energy difference between CBM and LVBM highlighted by the olive arrows is the band gap  $E_g$ , while the energy separations between LVBM and HVBM highlighted by orange arrows are labeled as  $\Delta\epsilon$ . (d) The comparison of  $E_g$  and  $\Delta\epsilon$  at 0 K among pristine, Cd-doped, and Hg-doped SnTe. The solid lines are guides to eye which show the variation tendencies of  $E_g$  and  $\Delta\epsilon$ .

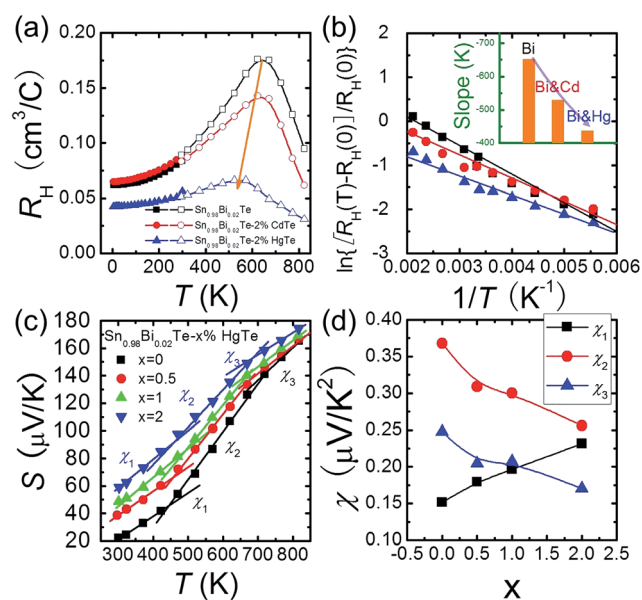


Fig. 5 (a) Temperature dependent Hall coefficient  $R_H$  for  $\text{Sn}_{0.98}\text{Bi}_{0.02}\text{Te}$ ,  $\text{Sn}_{0.98}\text{Bi}_{0.02}\text{Te}-2\%\text{CdTe}$ , and  $\text{Sn}_{0.98}\text{Bi}_{0.02}\text{Te}-2\%\text{HgTe}$ , the solid line is a guide to eye; (b)  $\ln[R_H(T) - R_H(0)]/R_H(0)$  as a function of  $1/T$  with the solid lines by best linearly fitting the data; inset of (b): slopes of the solid lines. (c) Three regions are obtained when modeling the Seebeck coefficients of the  $\text{Sn}_{0.98}\text{Bi}_{0.02}\text{Te}-x\%\text{HgTe}$  ( $x = 0-2$ ) samples using a linear temperature dependence. From low to mid and to high temperature range, the slopes of  $S-T$  plot ( $\chi$ ) are labeled as  $\chi_1$ ,  $\chi_2$ , and  $\chi_3$ , respectively. (d)  $\chi_1$ ,  $\chi_2$ , and  $\chi_3$  values as a function of  $x$ .

sufficiently low, almost all the charge carriers are within the light-hole band.<sup>56,57</sup> With increasing temperature,  $R_H$  increases gradually because of the temperature dependent band offset and the redistribution of carriers between the light-hole band and heavy-hole band.<sup>13,26,61</sup> Maxima of  $R_H$ , which is a sign of band convergence,<sup>13,26,61</sup> occur around 660 K, 645 K, and 573 K for  $\text{Sn}_{0.98}\text{Bi}_{0.02}\text{Te}$ ,  $\text{Sn}_{0.98}\text{Bi}_{0.02}\text{Te}-2\%\text{CdTe}$ , and  $\text{Sn}_{0.98}\text{Bi}_{0.02}\text{Te}-2\%\text{HgTe}$ , respectively. These decreased temperatures in CdTe- and HgTe-alloyed samples are indicative of diminished energy separations between the two valence bands at room temperature,<sup>26,61</sup> which is consistent with the band structure calculations.

It is intriguing to see that the three samples have different slopes of  $R_H$ - $T$  plot. Aukerman *et al.*<sup>62</sup> developed a model to analyze the high temperature Hall data of a typical two-conduction-band compound GaAs. In this model, the temperature dependent  $R_H(T)$  can be expressed as:

$$\frac{R_H(T) - R_H(0)}{R_H(0)} = \left(1 - \frac{\mu_2}{\mu_1}\right)^2 \left(\frac{m_2}{m_1}\right)^{3/2} e^{-\frac{\Delta\epsilon}{k_B T}} \quad (1)$$

where  $R_H(0)$  represents the Hall coefficient at 0 K,  $\mu_1$ ,  $\mu_2$ , and  $m_1$ ,  $m_2$  denote the mobilities and density of states effective masses of the first and the second conduction band, respectively,  $k_B$  is the Boltzmann constant, and  $\Delta\epsilon$  is the energy separation between the two conduction band minima. Here, we employ the same model to simulate the  $R_H(T)$  of p-type SnTe so as to better understand its two valence band nature. Since  $R_H(T)$  is nearly temperature independent below 150 K, we hypothesize that  $R_H(0) = R_H(5)$ . The  $\ln[R_H(T) - R_H(0)]/R_H(0)$  vs.  $1/T$  plots shown in Fig. 5(b) yield good linear dependences for the three samples, which indicates the reliability of the model. If we assume a linear temperature dependence of  $\Delta\epsilon$ ,<sup>57</sup> the slope of the  $\ln[R_H(T) - R_H(0)]/R_H(0)$  vs.  $1/T$  plot directly reflects the  $\Delta\epsilon$  at 0 K. As can be seen from inset of Fig. 5(b), the absolute values of slopes decrease from 651 K for Bi-doped SnTe, to 529 K for Bi&Cd co-doped SnTe, and to 436 K for Bi and Hg co-doped SnTe, suggesting a gradual decrease of  $\Delta\epsilon$ , which shows good consistency with the band structure calculations.

To understand the temperature dependence of the Seebeck coefficients of the Hg-alloyed samples, one can write the expressions for the diffusion Seebeck coefficient for degenerate doped semiconductors with parabolic dispersions as:<sup>57</sup>

$$S = \frac{2\pi^{2/3}k_B^2 m^*}{3^{5/3}e\hbar^2 N_p^{2/3}} \times \left(r + \frac{3}{2}\right) \times T \quad (2)$$

where  $h$  is the Plank constant,  $m^*$  is the density of states effective mass,  $N_p$  is the hole concentration, and  $r$  is the scattering exponent. Clearly, the slope of the  $S$ - $T$  plot,  $\chi$ , is primarily determined by the dependences of  $m^*$  and  $N_p$  on temperature. In the pristine sample SnTe (*i.e.* before band convergence has happened by alloying Hg),  $m^*$  increases with increasing temperature because of gradually increasing band convergence while  $N_p$  decreases ( $R_H$  increases, Fig. 5(a)) in this process, which means that  $\chi$  should increase with increasing  $T$ . After Hg is alloyed and band modification occurs, the heavy-hole band dominates and  $m^*$  is practically temperature independent,<sup>63</sup>

suggesting a decrease of  $\chi$  with increasing  $N_p$ . Indeed, modeling the Seebeck coefficients of  $\text{Sn}_{0.98}\text{Bi}_{0.02}\text{Te}-x\%\text{HgTe}$  with a linear temperature dependence roughly yields three different  $\chi$  values, namely  $\chi_1$ ,  $\chi_2$ , and  $\chi_3$  from low to middle and to high temperatures, Fig. 5(c). Fig. 5(d) shows  $\chi$  values as a function of  $x$  for  $\text{Sn}_{0.98}\text{Bi}_{0.02}\text{Te}-x\%\text{HgTe}$ . Evidently, all samples follow the same trend that  $\chi_1 < \chi_2$  while  $\chi_2 > \chi_3$ , which is consistent with above analysis. Moreover, one can see that  $\chi_1$  increases while both  $\chi_2$  and  $\chi_3$  decrease with increasing  $x$ .

As  $N_p$  increases with increasing  $x$  near room temperature (Fig. 1(c)), the increase of  $\chi_1$  is mainly attributed to the enhancement of  $m^*$  which can further support the band convergence hypothesis. Due to a weaker temperature dependence of  $R_H$  in Hg-alloyed samples, at elevated temperature, the  $N_p$  difference between  $\text{Sn}_{0.98}\text{Bi}_{0.02}\text{Te}$  and Hg-alloyed samples becomes more and more evident, Fig. 5(a). Under this circumstance, it is  $N_p$  that dominates  $\chi$ . Because of the increased  $N_p$  by Hg alloying (Fig. 1(c)),  $\chi_2$  and  $\chi_3$  decrease with increasing  $x$ , which can well explain the lack of Seebeck coefficient enhancement in the Hg-alloyed samples at high temperatures, which is different from the case of Cd-alloyed SnTe.<sup>33</sup>

### Thermal transport properties

The temperature dependent total thermal conductivities  $\kappa_{\text{tot}}$  for  $\text{Sn}_{0.98}\text{Bi}_{0.02}\text{Te}-x\%\text{HgTe}$  decrease with increasing temperature and increasing amount of HgTe, Fig. 6(a). The lattice thermal conductivity  $\kappa_{\text{lat}}$  can be obtained by removing the electronic component  $\kappa_{\text{ec}}$  from  $\kappa_{\text{tot}}$  using Wiedemann-Franz relation  $\kappa_{\text{ec}} = L\sigma T$ . The Lorenz number  $L$  is calculated by fitting the Seebeck coefficient data to the reduced chemical potential utilizing a single parabolic band model with acoustic phonon scattering.<sup>12,22</sup> This yields an  $L$  with a deviation of less than 10% as compared to a more rigorous single non-parabolic band and multiple band model calculation.<sup>64</sup>

The calculated  $(\kappa_{\text{tot}} - L\sigma T)$  for  $\text{Sn}_{0.98}\text{Bi}_{0.02}\text{Te}-x\%\text{HgTe}$ , first decreases with increasing temperature because of the phonon-phonon Umklapp scattering (U-scattering) and then increases at elevated temperature due to bipolar diffusion, Fig. 6(b). It is expected that at temperature above the Debye temperature ( $\Theta_D$ ,  $\sim 140$  K for SnTe<sup>65</sup>), for a semiconductor with U-scattering as the dominant phonon scattering mechanism,  $\kappa_{\text{lat}}$  should vary as  $1/T$ .<sup>66</sup> The portion that deviates from such a temperature dependence can be viewed as the bipolar diffusion contribution  $\kappa_{\text{bipolar}}$ , Fig. 6(c). The ratio of  $\kappa_{\text{bipolar}}/\kappa_{\text{tot}}$  at 823 K as a function of  $x$  for  $\text{Sn}_{0.98}\text{Bi}_{0.02}\text{Te}-x\%\text{HgTe}$  is illustrated in inset of Fig. 6(c). Clearly, the bipolar diffusion contribution to the total thermal conductivity decreases rapidly with increasing HgTe content, from a pronounced  $\sim 50\%$  for the sample with  $x = 0$  to a negligible  $\sim 3\%$  for the sample with  $x = 4$ . Because of the increased hole concentration upon HgTe alloying (Fig. 1(c)) we can expect a suppression of the bipolar conduction. Therefore both the band gap opening and increase in hole concentration together are likely contributing to the suppression. That the wider band gap of the Hg containing samples contributes to the bipolar conduction suppression is evident when we compare the two samples with  $x = 0$  and 1 having comparable hole

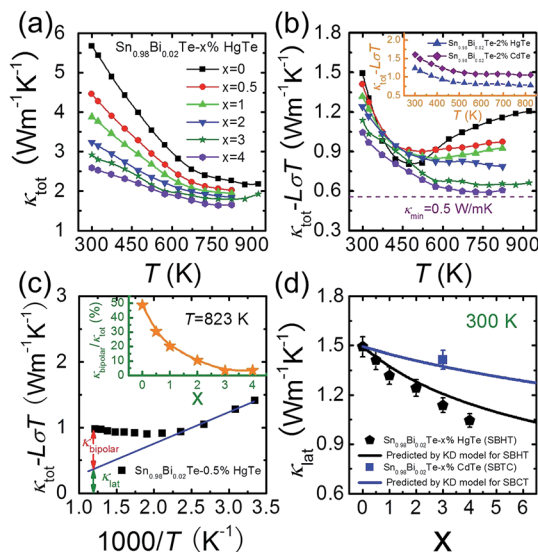


**Fig. 6** Temperature dependent (a) total thermal conductivity  $\kappa_{\text{tot}}$  and (b)  $(\kappa_{\text{tot}} - L\sigma T)$  for  $\text{Sn}_{0.98}\text{Bi}_{0.02}\text{Te}-x\%\text{HgTe}$  samples; the dotted line shows the theoretically lowest thermal conductivity based on the model proposed by Cahill *et al.*<sup>72</sup> inset of (b): a comparison of  $(\kappa_{\text{tot}} - L\sigma T)$  between  $\text{Sn}_{0.98}\text{Bi}_{0.02}\text{Te}-2\%\text{CdTe}$  and  $\text{Sn}_{0.98}\text{Bi}_{0.02}\text{Te}-2\%\text{HgTe}$ ; (c) an example which shows how to obtain the bipolar diffusion contribution to the total thermal conductivity by linearly fitting the  $(\kappa_{\text{tot}} - L\sigma T)$  vs.  $1000/T$  plot. Deviation of the thermal conductivity indicates a significant bipolar contribution; inset of (c): calculated  $\kappa_{\text{bipolar}}/\kappa_{\text{tot}}$  as a function of  $x$  which indicates that introduction of Hg can significantly suppress the bipolar diffusion; (d) room temperature lattice thermal conductivity  $\kappa_{\text{lat}}$  as a function of  $x$ . Error bars are indicated. The black and solid lines correspond to the prediction of Klemens–Drabble theory<sup>50,51</sup> on the lattice thermal conductivity of solid solution alloys for  $\text{Sn}_{0.98}\text{Bi}_{0.02}\text{Te}-x\%\text{HgTe}$  and  $\text{Sn}_{0.98}\text{Bi}_{0.02}\text{Te}-x\%\text{CdTe}$ , respectively.

densities ( $7.02$  vs.  $7.34 \times 10^{20} \text{ cm}^{-3}$ , Fig. 1(c)). The bipolar effect in the latter is largely lowered ( $\kappa_{\text{bipolar}}/\kappa_{\text{tot}}$  decreasing from  $\sim 50\%$  to  $\sim 30\%$ , Fig. 6(c)).

The room temperature ( $\kappa_{\text{tot}} - L\sigma T$ ) decreases with increasing HgTe amount, which, to a large extent, is attributed to the enhanced point defect scattering induced by Hg alloying. Also, one can see from the inset of Fig. 6(b) that at comparable doping amounts the HgTe-containing sample has a lower lattice thermal conductivity than the CdTe-containing one. This is attributed to the larger atomic radius and mass difference between Hg and Sn which could cause stronger point defect scattering.

The well-accepted Klemens–Drabble (KD) model<sup>67,68</sup> of disordered alloys was applied to predict the variation of lattice thermal conductivity of  $\text{Sn}_{0.98}\text{Bi}_{0.02}\text{Te}-x\%\text{HgTe/CdTe}$ . The required fitting parameters are adopted from references:  $\Theta_D$  of 140 K,<sup>65</sup> an average sound velocity of  $1800 \text{ m s}^{-1}$ ,<sup>69</sup> and atomic radii for Sn, Bi, Hg, Cd, and Te in a six-coordinate environment.<sup>70</sup> The main uncertainty in calculating lattice thermal conductivity lies in the determination of the phenomenological parameter  $\varepsilon$  which is a function of the Grüneisen parameter  $\gamma$ . Considering the similarity in crystal structure between SnTe and PbTe, in the present calculation, we used the same  $\varepsilon$  value ( $\sim 65$ ) as assumed for PbTe.<sup>71</sup>

The calculated lattice thermal conductivities as a function of  $x$  in light of the KD model are shown in Fig. 6(d). For the  $\text{Sn}_{0.98}\text{Bi}_{0.02}\text{Te}-x\%\text{HgTe}$  system, it can be seen that for the samples with  $x \leq 2$ , within error margin, the experimental values of  $\kappa_{\text{lat}}$  agree well with the theoretical prediction, suggesting point defect scattering being largely responsible for the reduction of  $\kappa_{\text{lat}}$ . However, when  $x \geq 3$ , the experimental  $\kappa_{\text{lat}}$  lies below the KD theory line, indicating other possible phonon scattering mechanisms in addition to point defect scattering, such as: mesoscale scattering *via* grain boundaries (GB),<sup>12</sup> and expected GB segregation of Hg which may also contribute to phonon impedance. Interestingly, for the  $\text{Sn}_{0.98}\text{Bi}_{0.02}\text{Te}-3\%\text{CdTe}$ , one can see that the experimental  $\kappa_{\text{lat}}$  is consistent with the simulated value using KD model, although PXRD unambiguously reveals the existence of CdTe second phase (Fig. S3†). Here, however, the CdTe second phase is too large in size (*i.e.*, not nanostructured), at much lower volume fraction and too isolated to efficiently scatter acoustic phonons.

Benefiting from the enhanced alloying scattering and bipolar diffusion suppression by the Hg alloying, as well as possible contribution *via* interfacial scattering of phonons by GBs, the minimum  $\kappa_{\text{lat}}$  is only  $\sim 0.6 \text{ Wm}^{-1} \text{ K}^{-1}$  at  $\sim 780$  K for the  $x = 4$  sample, which is close to the theoretically lowest lattice thermal conductivity  $\kappa_{\text{min}}$  ( $\sim 0.5 \text{ Wm}^{-1} \text{ K}^{-1}$ ) for SnTe-based material calculated using the model proposed by Cahill *et al.*<sup>72</sup>

$$\kappa_{\text{min}} = \frac{\pi}{4} k_B V^{-\frac{2}{3}} v \quad (3)$$

where  $V$  is the unit cell volume, and  $v$  is the average sound velocity. This is the lowest lattice thermal conductivity reported so far for SnTe-based materials.

### Electron microscopy characterizations of $\text{Sn}_{0.98}\text{Bi}_{0.02}\text{Te}-3\%\text{HgTe}$ and $\text{Sn}_{0.98}\text{Bi}_{0.02}\text{Te}-3\%\text{CdTe}$

The microstructure of the specimen, encompassing the crystallography, grain structure and composition analysis, was investigated by high resolution TEM (HRTEM), STEM and STEM EDS.

Fig. 7 shows the STEM observations of the  $\text{Sn}_{0.98}\text{Bi}_{0.02}\text{Te}-3\%\text{HgTe}$  specimen. The presence of the meso-scale grains with size ranging from  $0.4 \mu\text{m}$  to  $2 \mu\text{m}$  are shown in Fig. 7(a). The meso-scale microstructure is generated by the SPS treatment. The medium magnification TEM images under varied diffraction conditions show uniform contrast, which suggests no nano-scale precipitates in the matrix. The inset figure at the upper right corner of Fig. 7(b) is a HRTEM image along  $[11\bar{2}]$  zone axis and the corresponding selected area diffraction (SAD) pattern is shown at the lower right corner in Fig. 7(b). However, larger size Hg-rich particles are found to preferentially occupy at the grain boundaries (and triple junctions) as shown in Fig. S6†. The occurrence of the large Hg rich particles is consistent with the PXRD result, as shown in Fig. 1(a). STEM EDS characterizes the composition of the specimen as shown in Fig. 7(c). Sn, Te, Hg and Bi peaks were identified in the spectrum. An enlarged inset figure in Fig. 7(c) shows clear Hg L1 and L $\alpha$  peaks. Large Hg rich particles cannot scatter phonons effectively *via* interface scattering, therefore point defects scattering due to the Hg alloying



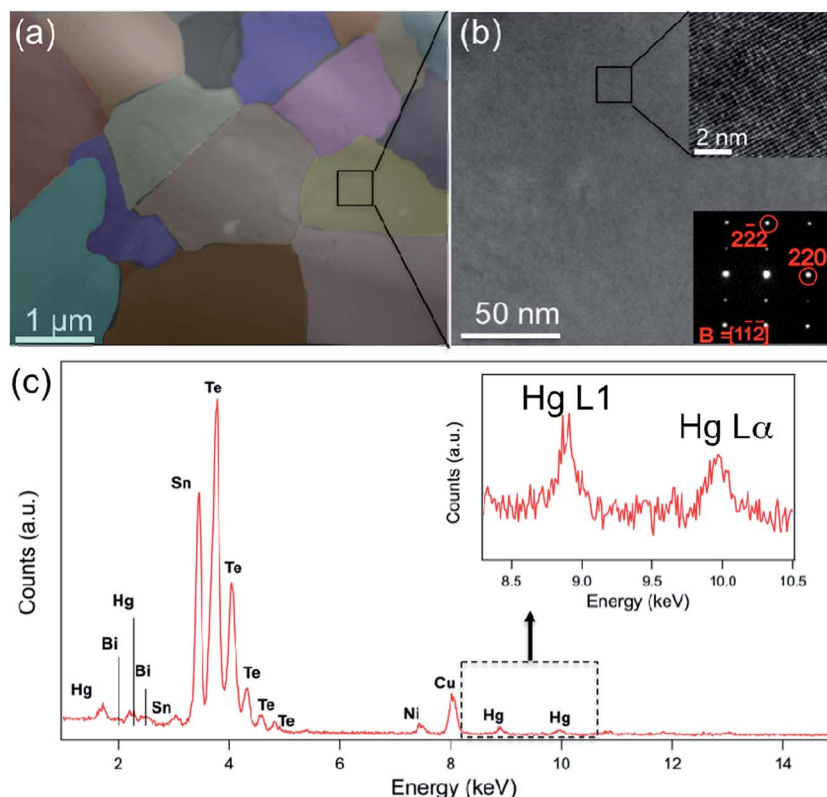


Fig. 7 Electron microscopy of  $\text{Sn}_{0.98}\text{Bi}_{0.02}\text{Te}-3\%\text{HgTe}$ : (a) a low-magnification TEM image shows mesoscale uniform microstructure of the specimen. The color of the grains was modified for a better view. (b) A medium-magnification TEM image shows no nanoscale precipitates in the specimen. The inset figure on the upper right corner of (b) is a HRTEM image taken along  $[1\bar{1}2]$  direction. The inset figure on the lower right corner is the corresponding SAD pattern. (c) A STEM EDS shows Sn, Te, Hg and Bi peaks. The inset figure shows an enlarged Hg L1 and  $L\alpha$  peaks. Ni peak comes from the TEM grid and Cu peak is from the TEM holder.

is the main reason for small lattice thermal conductivity as shown in Fig. 6(b). We also note possible smaller contribution from mesoscale GB scattering and expected Hg-segregation at GBs and triple junctions. However, given microscale grain size, its contribution is likely to be smaller than the pervasive solid solution effect of Hg in SnTe.

We also compare the microstructure between  $\text{Sn}_{0.98}\text{Bi}_{0.02}\text{Te}-3\%\text{HgTe}$  and  $\text{Sn}_{0.98}\text{Bi}_{0.02}\text{Te}-3\%\text{CdTe}$ . STEM observations of the  $\text{Sn}_{0.98}\text{Bi}_{0.02}\text{Te}-3\%\text{CdTe}$  specimen are shown in Fig. 8. A low magnification STEM image in Fig. 8(a) shows a  $\sim 150$  nm CdTe precipitate with dark contrast embedding in the matrix, which is similar to the case in PbTe–CdTe system.<sup>61</sup> An HRTEM image of the CdTe/matrix interface is shown in Fig. 8(b). The Moiré fringes at the interface are due to the lattice overlap of CdTe and the matrix. STEM EDS was used to reveal the composition of the CdTe second phase. Only Cd and Te signals are found in the CdTe precipitate, and no Sn peak was observed. In the matrix, the Cd peak is not observable, likely because the amount of Cd is too small to be detected by STEM EDS. The CdTe precipitates are coarse and large enough to be detected by PXRD, as shown in Fig. S3.† Also, we observe the scarce distribution and rather large size of CdTe precipitates make them inefficient at impeding the phonon propagation. This is why no obvious reduction in lattice thermal conductivity is observed when Cd exceeds its solubility limit in the

$\text{Sn}_{1.03-x}\text{Cd}_x\text{Te}$  system<sup>33</sup> and no additional lattice thermal conductivity reduction is seen when CdTe precipitates from the  $\text{Sn}_{0.98}\text{Bi}_{0.02}\text{Te}-3\%\text{CdTe}$  sample, as shown in Fig. 6(d). The reduction in the lattice thermal conductivity of HgTe-containing SnTe (due to point defects of Hg in the SnTe matrix) is much more significant than the reduction in the lattice thermal conductivity of the CdTe-containing sample. Nevertheless, large particles of HgTe are also formed (Fig. S6†) when the solubility limits of Hg in SnTe are exceeded.

### ZT values

Fig. 9(a) plots the thermoelectric figure of merit  $ZT$  as a function of temperature for  $\text{Sn}_{0.98}\text{Bi}_{0.02}\text{Te}-x\%\text{HgTe}$ . The  $ZT$ s increase with increasing temperature and HgTe content, with the highest value reaching  $\sim 1.35$  at 923 K for the sample with  $x = 3$ . This is  $\sim 50\%$  improvement over the pristine  $\text{Sn}_{0.98}\text{Bi}_{0.02}\text{Te}$  sample and 30% higher than that of  $\text{Sn}_{0.98}\text{Bi}_{0.02}\text{Te}-3\%\text{CdTe}$  ( $ZT \sim 1.05$  at 870 K). This enhancement of  $ZT$  mainly originates from the significantly improved power factor and greatly lowered lattice thermal conductivity *via* HgTe alloying. This value is also slightly higher than what we obtained in the  $\text{SnCd}_{0.03}\text{Te}-x\%\text{CdS}$  system<sup>33</sup> and much superior to that of In-doped SnTe.<sup>27</sup> More importantly, a great enhancement of  $ZT_{\text{ave}}$  has been achieved. Specifically, the  $ZT_{\text{ave}}$  values between 300 and 900 K are 0.55,

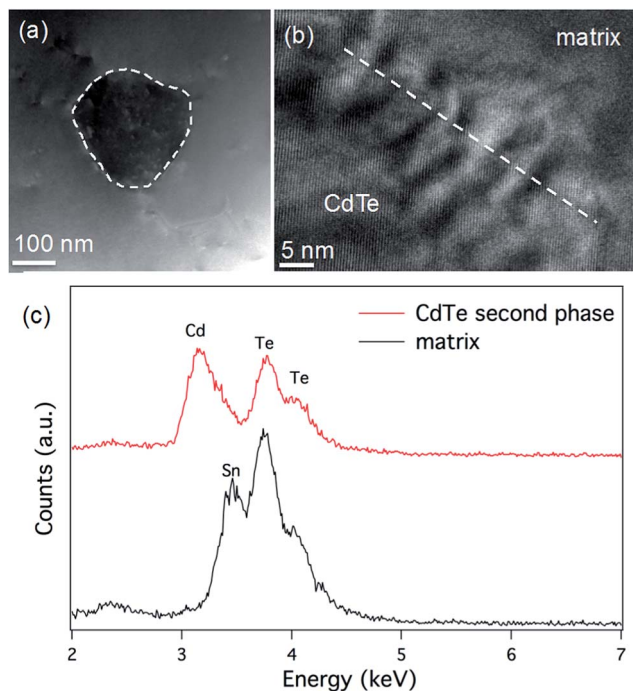


Fig. 8 Electron microscopy of  $\text{Sn}_{0.98}\text{Bi}_{0.02}\text{Te}-3\%\text{CdTe}$ : (a) a low magnification STEM image shows an embedded CdTe precipitate in the matrix with dark contrast compared to the surrounded matrix; (b) HRTEM image of the interface between CdTe precipitate and the matrix; (c) STEM-EDX shows significant difference between the precipitate and the matrix: Cd and Te signals are found in the precipitate but no Sn signal was found within the experimental conditions employed.

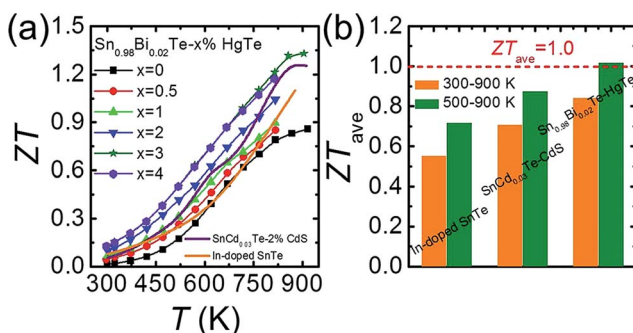


Fig. 9 (a) Temperature dependent  $ZT$  values for  $\text{Sn}_{0.98}\text{Bi}_{0.02}\text{Te}-x\%\text{HgTe}$  and  $\text{Sn}_{0.98}\text{Bi}_{0.02}\text{Te}-3\%\text{CdTe}$  in comparison with the reported data on In-doped  $\text{SnTe}$ <sup>27</sup> and Cd-doped  $\text{SnTe}$  nanostructured with  $\text{CdS}$ <sup>33</sup>; (b) a comparison of average  $ZT$  ( $ZT_{\text{ave}}$ ) of 300–900 K and 500–900 K among In-doped  $\text{SnTe}$ ,<sup>27</sup>  $\text{SnCd}_{0.03}\text{Te}-2\%\text{CdS}$ ,<sup>33</sup> and  $\text{Sn}_{0.98}\text{Bi}_{0.02}\text{Te}-3\%\text{HgTe}$ .

0.71, and 0.84 for In-doped  $\text{SnTe}$ ,  $\text{SnCd}_{0.03}\text{Te}-2\%\text{CdS}$ , and  $\text{Sn}_{0.98}\text{Bi}_{0.02}\text{Te}-3\%\text{HgTe}$ , respectively, while those between 500 and 900 K are 0.72, 0.87, and 1.02, respectively, Fig. 9(b). This is comparable to the  $ZT_{\text{ave}}$  of the recently reported  $\text{SnSe}$  single crystals for the same temperature range.<sup>73</sup> We note that a significant enhancement of  $ZT_{\text{ave}}$  is of greater value to overall thermoelectric conversion efficiency than just increasing the maximum value of  $ZT$ .<sup>74</sup> Although we have not performed

systematic studies, we found that the high performance material is quite stable even after heating at 723 K for 7 d in vacuum, see Fig. S7.†

## 4. Concluding remarks

The introduction of Hg in the Sn-site of  $\text{SnTe}$  is effective in achieving valence band convergence, giving rise to a great enhancement of the Seebeck coefficient and the power factor. Due to the large differences in atomic radii and mass contrast between Hg and Sn, strong point defect scattering is apparent upon  $\text{HgTe}$  alloying, which along with contributions from mesoscale GBs results in a noticeable reduction of lattice thermal conductivity. In conjunction with the bipolar diffusion suppression due to band gap opening by Hg alloying, the  $\text{Sn}_{0.98}\text{Bi}_{0.02}\text{Te}-x\%\text{HgTe}$  system possesses a very low lattice thermal conductivity. The multiply favorable roles that Hg plays in regulating the electron and phonon transport of  $\text{SnTe}$  lead to a maximum  $ZT$  of 1.35 at  $\sim 910$  K and more importantly, a largely enhanced average  $ZT$  in  $\text{Sn}_{0.98}\text{Bi}_{0.02}\text{Te}-x\%\text{HgTe}$ . This work suggests that  $\text{SnTe}$ -based materials are viable candidates for thermoelectric power generation.

## Acknowledgements

This work was supported as part of the Revolutionary Materials for Solid State Energy Conversion, an Energy Frontier Research Center funded by the U.S. Department of Energy, Office of Science, and Office of Basic Energy Sciences under Award Number DE-SC0001054. Transmission electron microscopy work was partially performed in the EPIC facility of the NUANCE Center at Northwestern University.

## References

- (a) F. J. DiSalvo, *Science*, 1999, **285**, 703–706; (b) L.-D. Zhao, V. P. Dravid and M. G. Kanatzidis, *Energy Environ. Sci.*, 2014, **7**, 251–268; (c) J. He, M. G. Kanatzidis and V. P. Dravid, *Mater. Today*, 2013, **16**, 166–176.
- (a) L. E. Bell, *Science*, 2008, **321**, 1457–1461; (b) M. G. Kanatzidis, *Chem. Mater.*, 2010, **22**, 648–659.
- T. M. Tritt, *Science*, 1999, **283**, 804–805.
- J. Yang and T. Caillat, *MRS Bull.*, 2006, **31**, 224–229.
- F. Rosi, *Solid-State Electron.*, 1968, **11**, 833–868.
- J.-P. Fleurial, *JOM*, 2009, **61**, 79–85.
- T. D. Barr and F. Dahlen, *J. Geophys. Res.: Solid Earth*, 1989, **94**, 3923–3947.
- C.-T. Hsu, G.-Y. Huang, H.-S. Chu, B. Yu and D.-J. Yao, *Appl. Energy*, 2011, **88**, 1291–1297.
- C. Wu, *Appl. Therm. Eng.*, 1996, **16**, 63–69.
- K. F. Hsu, S. Loo, F. Guo, W. Chen, J. S. Dyck, C. Uher, T. Hogan, E. Polychroniadis and M. G. Kanatzidis, *Science*, 2004, **303**, 818–821.
- J. P. Heremans, V. Jovovic, E. S. Toberer, A. Saramat, K. Kurosaki, A. Charoenphakdee, S. Yamanaka and G. J. Snyder, *Science*, 2008, **321**, 554–557.

- 12 K. Biswas, J. He, I. D. Blum, C.-I. Wu, T. P. Hogan, D. N. Seidman, V. P. Dravid and M. G. Kanatzidis, *Nature*, 2012, **489**, 414–418.
- 13 Y. Pei, X. Shi, A. LaLonde, H. Wang, L. Chen and G. J. Snyder, *Nature*, 2011, **473**, 66–69.
- 14 R. J. Korkosz, T. C. Chasapis, S.-H. Lo, J. W. Doak, Y. J. Kim, C.-I. Wu, E. Hatzikraniotis, T. P. Hogan, D. N. Seidman and C. Wolverton, *J. Am. Chem. Soc.*, 2014, **136**, 3225–3237.
- 15 J. Androulakis, I. Todorov, J. He, D.-Y. Chung, V. Dravid and M. Kanatzidis, *J. Am. Chem. Soc.*, 2011, **133**, 10920–10927.
- 16 J. R. Sootsman, H. Kong, C. Uher, J. J. D'Angelo, C. I. Wu, T. P. Hogan, T. Caillat and M. G. Kanatzidis, *Angew. Chem.*, 2008, **120**, 8746–8750.
- 17 L.-D. Zhao, J. He, C.-I. Wu, T. P. Hogan, X. Zhou, C. Uher, V. P. Dravid and M. G. Kanatzidis, *J. Am. Chem. Soc.*, 2012, **134**, 7902–7912.
- 18 B. Sales, D. Mandrus and R. K. Williams, *Science*, 1996, **272**, 1325–1328.
- 19 X. Shi, J. Yang, J. R. Salvador, M. Chi, J. Y. Cho, H. Wang, S. Bai, J. Yang, W. Zhang and L. Chen, *J. Am. Chem. Soc.*, 2011, **133**, 7837–7846.
- 20 G. Rogl, A. Grytsiv, P. Rogl, N. Peranio, E. Bauer, M. Zehetbauer and O. Eibl, *Acta Mater.*, 2014, **63**, 30–43.
- 21 Y. Qiu, L. Xi, X. Shi, P. Qiu, W. Zhang, L. Chen, J. R. Salvador, J. Y. Cho, J. Yang and Y. C. Chien, *Adv. Funct. Mater.*, 2013, **23**, 3194–3203.
- 22 G. Tan, W. Liu, H. Chi, X. Su, S. Wang, Y. Yan, X. Tang, W. Wong-Ng and C. Uher, *Acta Mater.*, 2013, **61**, 7693–7704.
- 23 J. Yao, N. J. Takas, M. L. Schliefer, D. S. Paprocki, P. E. Blanchard, H. Gou, A. Mar, C. L. Exstrom, S. A. Darveau and P. F. Poudeu, *Phys. Rev. B: Condens. Matter Mater. Phys.*, 2011, **84**, 075203.
- 24 J. Y. Cho, X. Shi, J. Salvador, J. Yang and H. Wang, *J. Appl. Phys.*, 2010, **108**, 073713.
- 25 R. Liu, L. Xi, H. Liu, X. Shi, W. Zhang and L. Chen, *Chem. Commun.*, 2012, **48**, 3818–3820.
- 26 L. Zhao, H. Wu, S. Hao, C. Wu, X. Zhou, K. Biswas, J. He, T. Hogan, C. Uher and C. Wolverton, *Energy Environ. Sci.*, 2013, **6**, 3346–3355.
- 27 Q. Zhang, B. Liao, Y. Lan, K. Lukas, W. Liu, K. Esfarjani, C. Opeil, D. Broido, G. Chen and Z. Ren, *Proc. Natl. Acad. Sci. U. S. A.*, 2013, **110**, 13261–13266.
- 28 Y. Chen, M. D. Nielsen, Y. B. Gao, T. J. Zhu, X. Zhao and J. P. Heremans, *Adv. Energy Mater.*, 2012, **2**, 58–62.
- 29 D. J. Singh, *Funct. Mater. Lett.*, 2010, **3**, 223–226.
- 30 M. K. Han, J. Androulakis, S. J. Kim and M. G. Kanatzidis, *Adv. Energy Mater.*, 2012, **2**, 157–161.
- 31 R. Brebrick and A. Strauss, *Phys. Rev.*, 1963, **131**, 104.
- 32 S. Rabii, *Phys. Rev.*, 1969, **182**, 821.
- 33 G. Tan, L.-D. Zhao, F. Shi, J. W. Doak, S.-H. Lo, H. Sun, C. Wolverton, V. P. Dravid, C. Uher and M. G. Kanatzidis, *J. Am. Chem. Soc.*, 2014, **136**, 7006–7017.
- 34 P. Hohenberg and W. Kohn, *Phys. Rev.*, 1964, **136**, B864.
- 35 W. Khon and L. Sham, *Phys. Rev.*, 1965, **140**, A1133–A1138.
- 36 G. Kresse and J. Hafner, *Phys. Rev. B: Condens. Matter Mater. Phys.*, 1993, **47**, 558.
- 37 G. Kresse and J. Hafner, *Phys. Rev. B: Condens. Matter Mater. Phys.*, 1994, **49**, 14251.
- 38 G. Kresse and J. Furthmüller, *Phys. Rev. B: Condens. Matter Mater. Phys.*, 1996, **54**, 11169.
- 39 G. Kresse and J. Furthmüller, *Comput. Mater. Sci.*, 1996, **6**, 15–50.
- 40 P. E. Blöchl, *Phys. Rev. B: Condens. Matter Mater. Phys.*, 1994, **50**, 17953.
- 41 J. P. Perdew, K. Burke and M. Ernzerhof, *Phys. Rev. Lett.*, 1996, **77**, 3865.
- 42 G. Kresse and D. Joubert, *Phys. Rev. B: Condens. Matter Mater. Phys.*, 1999, **59**, 1758.
- 43 J. E. Saal, S. Kirklin, M. Aykol, B. Meredig and C. Wolverton, *JOM*, 2013, **65**, 1501–1509.
- 44 S. Lany and A. Zunger, *Modell. Simul. Mater. Sci. Eng.*, 2009, **17**, 084002.
- 45 Y. N. Nasirov, N. Sultanova and T. Osmanov, *Phys. Status Solidi B*, 1969, **35**, K39–K42.
- 46 K. Biswas, J. He, G. Wang, S.-H. Lo, C. Uher, V. P. Dravid and M. G. Kanatzidis, *Energy Environ. Sci.*, 2011, **4**, 4675–4684.
- 47 J. Androulakis, Y. Lee, I. Todorov, D.-Y. Chung and M. Kanatzidis, *Phys. Rev. B: Condens. Matter Mater. Phys.*, 2011, **83**, 195209.
- 48 V. P. Vedenev, S. P. Krivoruchko and E. P. Sabo, *Semiconductors*, 1998, **32**, 241–244.
- 49 M. Galushchak, D. Freik, I. Ivanyshyn, A. Lisak and M. Pyts, *J. Thermoelectr.*, 2000, 42–50.
- 50 J. Kafalas, R. Brebrick and A. Strauss, *Appl. Phys. Lett.*, 1964, **4**, 93–94.
- 51 N. Wang, D. West, J. Liu, J. Li, Q. Yan, B.-L. Gu, S. Zhang and W. Duan, *Phys. Rev. B: Condens. Matter Mater. Phys.*, 2014, **89**, 045142.
- 52 C. Okoye, *J. Phys.: Condens. Matter*, 2002, **14**, 8625.
- 53 L. Esaki and P. Stiles, *Phys. Rev. Lett.*, 1966, **16**, 1108.
- 54 J. Dimmock, I. Melngailis and A. Strauss, *Phys. Rev. Lett.*, 1966, **16**, 1193.
- 55 The electronic DOS of Cd-doped SnTe has been previously calculated, where it was also found that the Cd defect opened the band gap of SnTe and created an impurity band within the band gap of SnTe [S. Ahmad, *Adv. Mater. Res.*, 2013, **701**, 125]. However, they incorrectly placed the Fermi level of the calculation above this impurity level, suggesting that the Cd impurity band should be filled. In contrast, we find that the Fermi level [dotted line in Fig. 4(b)] lies below the impurity band [dashed line in Fig. 4(b)], suggesting that the effects of Cd on the transport properties of SnTe should be related to the modification of the valence band, as opposed to resonant-level enhancement [J. P. Heremans *et al.*, *Science*, 2008, **321**, 554–557].
- 56 R. S. Allgaier and B. B. Houston, *J. Appl. Phys.*, 1966, **37**, 302–309.
- 57 I. U. R. I. Ravich, B. A. E. Efimova and I. A. Smirnov, *Semiconducting lead chalcogenides*, Plenum Publishing Corporation, 1970.
- 58 A. Andreev and V. Radionov, *Soviet Physics Semiconductors*, 1967, **1**, 145–148.

- 59 I. Chernik, V. Kaidanov, M. Vinogradova and N. Kolomoets, *Soviet Physics Semiconductors*, 1968, **2**, 645–651.
- 60 J. Androulakis, I. Todorov, D.-Y. Chung, S. Ballikaya, G. Wang, C. Uher and M. Kanatzidis, *Phys. Rev. B: Condens. Matter Mater. Phys.*, 2010, **82**, 115209.
- 61 Y. Pei, A. D. LaLonde, N. A. Heinz and G. J. Snyder, *Adv. Energy Mater.*, 2012, **2**, 670–675.
- 62 L. Aukerman and R. Willardson, *J. Appl. Phys.*, 1960, **31**, 939–940.
- 63 Y. Pei, A. LaLonde, S. Iwanaga and G. J. Snyder, *Energy Environ. Sci.*, 2011, **4**, 2085–2089.
- 64 M. Vinograd, N. Kolomoet, I. Smirnov and L. Sysoeva, *Soviet Physics Semiconductors*, 1968, **9**, 2368.
- 65 S. Bukshpan, *Solid State Commun.*, 1968, **6**, 477–478.
- 66 G. S. Nolas, J. Sharp and J. Goldsmid, *Thermoelectrics: basic principles and new materials developments*, Springer, 2001.
- 67 T. Irie, *Jpn. J. Appl. Phys.*, 1966, **5**, 854–859.
- 68 J. Yang, G. Meisner and L. Chen, *Appl. Phys. Lett.*, 2004, **85**, 1140–1142.
- 69 P. Bauer Pereira, I. Sergueev, S. Gorsse, J. Dadda, E. Müller and R. P. Hermann, *Phys. Status Solidi B*, 2013, **250**, 1300–1307.
- 70 R. Shannon, *Acta Crystallogr., Sect. A: Found. Crystallogr.*, 1976, **32**, 751–767.
- 71 G. Alekseeva, B. Efimova, L. Ostrovskaya, O. Serebryannikova and M. Tsy-pin, *Soviet Physics Semiconductors*, 1971, **4**, 1122–1125.
- 72 D. G. Cahill, S. K. Watson and R. O. Pohl, *Phys. Rev. B: Condens. Matter Mater. Phys.*, 1992, **46**, 6131.
- 73 L.-D. Zhao, S.-H. Lo, Y. Zhang, H. Sun, G. Tan, C. Uher, C. Wolverton, V. P. Dravid and M. G. Kanatzidis, *Nature*, 2014, **508**, 373–377.
- 74 H. J. Wu, L. D. Zhao, F. S. Zheng, D. Wu, Y. L. Pei, X. Tong, M. G. Kanatzidis and J. He, *Nat. Commun.*, 2014, **5**, 4515.